

Oscillating soliton molecules induced by strong vector-mode couplingJingyi Li, Dong Mao ^{*}, Qun Gao, Zhiwen He, Yueqing Du, Chao Zeng, and Jianlin Zhao *Key Laboratory of Light Field Manipulation and Information Acquisition, Ministry of Industry and Information Technology, Shaanxi Key Laboratory of Optical Information Technology and School of Physical Science and Technology, Northwestern Polytechnical University, Xi'an 710129, China*

(Received 24 September 2022; accepted 30 January 2023; published 9 February 2023)

Soliton molecules, composed of closely spaced pulses with strong internal interactions, have been in-depth studied in fiber lasers due to their fascinating evolution dynamics and potential applications in high-speed optical communications. Here we demonstrate a type of oscillating soliton molecules in a mode-locked fiber laser constituted by single-mode and polarization-maintaining fibers. Ascribing to the unequal coupling between two orthogonal-polarized vector modes, the constituent pulses of soliton molecules possess different intensities and further result in a dual-roundtrip and large-period oscillation. Numerical simulations reproduce the critical experimental phenomena and show that two vector modes display diverse departing behavior in polarization-maintaining fiber. This work sheds light on the role of strong birefringence on vector solitons, providing a flexible nonlinear system to generate and study oscillating soliton molecules.

DOI: [10.1103/PhysRevA.107.023508](https://doi.org/10.1103/PhysRevA.107.023508)**I. INTRODUCTION**

Solitons, as nondiffusive localized structures in nonlinear systems, are extensively studied in the fields of fluid mechanics [1], biology [2], plasma physics [3], and optics [4,5]. In optical fibers, solitons result from the delicate balance between anomalous dispersion and the self-phase modulation effect. A mode-locked fiber laser provides an ideal testbed for exploring dissipative solitons that arise from the complex interaction between Kerr nonlinearity, chromatic dispersion, gain, and loss [6]. Attributed to the law of survival of the strongest [7], mode-locked fiber lasers often emit a single soliton at the weak pump state. With the increase of pump strength, single-pulse operation evolves to a multi-pulse state owing to the peak-power-limiting effect of the cavity [8,9]. Under the complex interactions, these pulses form various self-organized structures [10], such as harmonic mode-locking [11], soliton rain [12,13], optical rogue wave [14], and soliton molecules (SMs) [15,16].

The formation mechanism of SMs has been theoretically revealed by solving the complex Ginzburg-Landau equations [17,18]. Through strong coherent interaction of the trailing fields, several solitons can form tightly bounded SMs in fibers or fiber lasers [19–24]. In analogy to matter molecules, SMs display intriguing properties, including vibrations, synthesis, and collision [25]. The SMs are stable during propagation in fibers, which is desirable for soliton communications [26]. Benefiting from the dispersive Fourier transform (DFT) technique that maps the pulses from the frequency domain to the temporal domain [27,28], the transient evolution and internal dynamics of SMs have been studied deeply in mode-locked fiber lasers. The SMs can be classified based on their trajectories in the phase space, composed of the separation and

phase difference between two pulses. Generally, the phase-locked SMs are represented by a fixed-point attractor in the phase space [29–31]. Via adjusting the polarization angle or saturation energy of the system to particular values, the fixed-point attractor destabilizes and transforms into the limit cycle by Hopf-type bifurcation, resulting in the oscillating SMs [32–35].

It is well known that birefringence is inevitable in single-mode fibers (SMFs), and the vector characteristics should be considered during pulse propagation in fiber lasers. Group-velocity-locked [36], polarization-locked [37], and polarization-rotated [38] vector soliton molecules (VSMs) have been found in SMF lasers. Compared with scalar SMs [9], the coupling between two orthogonal-polarized components of VSMs leads to more complex evolution dynamics, which is mainly determined by the cavity birefringence and mode-coupling strength [39,40]. The intracavity birefringence was relatively weak in previous studies [41], leaving VSMs less addressed in birefringence-managed fiber lasers consisting of SMFs and polarization-maintaining fibers (PMFs). Here, we demonstrate a type of oscillating soliton molecule (OSM) with intriguing internal dynamics in a near-zero-dispersion SMF-PMF laser. The OSMs consist of two pulses with varying intensities that are directly visualized by the DFT technique. Numerical simulation verifies the experimental observation, confirming that the strong coupling and departing of two vector modes determine the dual-roundtrip and large-period oscillations of SMs.

II. EXPERIMENTAL SETUP AND RESULT

Figure 1(a) illustrates the configuration of the SMF-PMF laser, comprising 3.8 m erbium-doped fiber (EDF), 0.9 m PMF, and 4.5 m SMF with dispersion parameters of $-18.5 \text{ ps (nm km)}^{-1}$, $17 \text{ ps (nm km)}^{-1}$, and $17 \text{ ps (nm km)}^{-1}$. The cavity length is 9.2 m, with a net

^{*}Corresponding author: maodong@nwpu.edu.cn

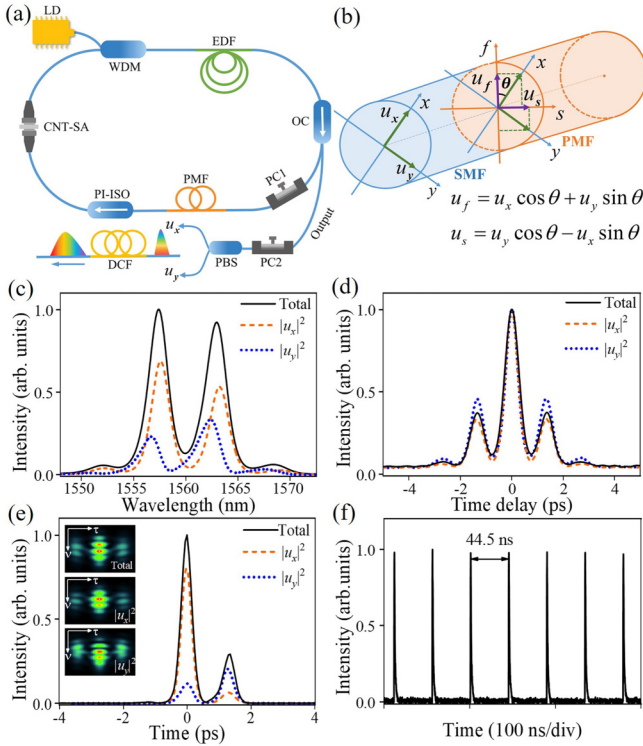


FIG. 1. Experimental setup and observations of OSM in SMF-PMF laser. (a) Configuration of the fiber laser. LD: laser diode; WDM: wavelength division multiplexer; EDF: erbium-doped fiber; OC: output coupler; PMF: polarization-maintaining fiber; PC: polarization controller; PI-ISO: polarization-insensitive isolator; CNT-SA: carbon nanotube saturable absorber; PBS: polarization beam splitter; DCF: dispersion-compensating fiber. (b) Coupling behavior of pulse from SMF to PMF. u_x (u_f) and u_y (u_s) are two orthogonal-polarized components in SMF (PMF). θ is the angle between the u_x and u_f components. (c) Optical spectra, (d) autocorrelation traces, (e) retrieved FROG spectrograms and pulse profiles, and (f) pulse trains. [Total: the solid black lines; u_x components: the dashed orange lines; u_y components: the dotted blue lines.]

dispersion of -0.027 ps^2 . The laser diode (LD) pumps EDF through a 980/1550 nm wavelength division multiplexer. The polarization-insensitive isolator ensures the unidirectional operation of the laser, and the carbon nanotube saturable absorber (CNT-SA) initiates the passive mode-locking operation. The laser beam is extracted by the optical coupler with a splitting ratio of 9:1 and monitored by an optical spectrum analyzer (Yokogawa, AQ6370), an autocorrelator (Pulsecheck, USB-150), a radio frequency analyzer (Agilent, E4440A), as well as a frequency-resolved optical gating (FROG, Femto Easy, FS-600). The DFT measurement is implemented by stretching the output pulses through a 5-km dispersion-compensation fiber (DCF), giving a total dispersion of $\sim 750 \text{ ps/nm}$. The broadened pulses are detected and recorded by a 5-GHz photodetector and a 4-GHz digital oscilloscope (LeCroy, 740Zi-A), respectively. The spectral resolution of the DFT system is estimated to be 0.83 nm. Two orthogonal-polarized components of OSMs are resolved by a polarization beam splitter (PBS) with a polarization controller (PC2) and measured separately by the above devices.

As shown in Fig. 1(b), the pulse in SMF can be split in orthogonal-polarized u_x and u_y components. When the pulse propagates from SMF to PMF, the angle between the u_x and u_f components determines the coupling behavior of two vector modes, and the u_x and u_y components of pulses evolve to fast (u_f) and slow (u_s) components following equations in the inset to Fig. 1(b). In the experiment, the polarization orientation can be tuned with the in-line polarization controller (PC1).

The self-starting mode-locking state is first established at the pump power of 15 mW. As shown in Appendix A, the pulses display a broad and smooth spectrum, which is typical for the stretched pulses in the near-zero dispersion regime [42]. Without changing the pump power, OSM can be obtained by slightly tuning the polarization controller before the PMF [Figs. 1(c)–1(f)]. The spectrum of OSM displays precise modulation with a period of 5.52 nm. Two orthogonal-polarized components exhibit the same spectral modulation period with a wavelength shift of $\sim 0.95 \text{ nm}$, which partially compensates for the polarization mode dispersion induced by the fiber birefringence [41]. In contrast to standard SMs composed of two identical pulses [9,43], the OSM is composed of two pulses with unequal intensity, as indicated by the autocorrelation traces [Fig. 2(d)], where the secondary peaks are less than half of the central peak. We further retrieve the profiles of the OSM and its two components from the FROG spectrograms [inset of Fig. 1(e)]. The unequal dual pulses have a separation of 1.35 ps, which agrees with the autocorrelation trace and spectral modulation. The pulse train shown in Fig. 1(f) gives the pulse-pulse separation of 44.5 ns, which is consistent with the 9.2-m cavity length and indicates the stable mode-locking state.

Through the DFT technique, we record the real-time evolution of spectra and field autocorrelation (FAC) traces of OSMs as a function of roundtrips (RTs). As shown in Fig. 2(a), the spectra and energy oscillate continuously with a period of 29 RTs. However, the spectral and temporal separations remain constant during the oscillation [Fig. 2(b)]. Two orthogonal-polarized components show a similar evolution pattern with the fixed temporal separations, as shown in Figs. 2(c)–2(f). The large-period oscillations consist of the dual-roundtrip oscillations in which the pulse intensity changes significantly in the temporal and spectral domain per two RTs. From the energy evolutions in Figs. 2(d) and 2(f), two components oscillate synchronously to each other for the large oscillation period of 29 RTs. However, the u_x and u_y components oscillate inversely during the small-period oscillation, and we infer an energy exchange between the u_x and u_y components per RT. The average spectra and FAC traces (upper panel of Fig. 2) over 600–700 RTs are consistent with the observation of Fig. 1 and further prove the reliability of the DFT technique.

III. SIMULATION AND DISCUSSION

Based on the known propagation model that takes into account the action of each component [8], we simulate the formation and evolution behaviors of OSM in the fiber laser from a weak noise pulse. In SMF and PMF, the pulse propagation is described by the complex Ginzburg-Landau equations [44,45]

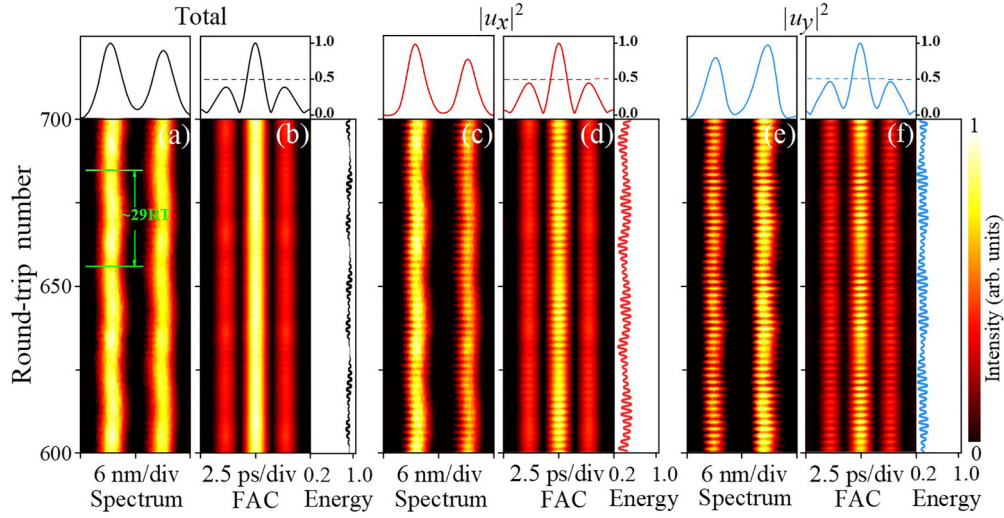


FIG. 2. Real-time evolution of OSMs over 600–700 roundtrips. Spectra and FAC traces of (a), (b) total pulse, (c), (d) u_x component, and (e), (f) u_y component. Upper panels show the averaged spectra and FAC traces. Right panels of (b), (d), and (f) show the evolution of the normalized energy.

and is solved by the symmetrical split-step Fourier method [46]:

$$\begin{aligned} \frac{\partial u_x}{\partial z} = & -i\beta u_x + \delta \frac{\partial u_x}{\partial t} - i\frac{\beta_2}{2} \frac{\partial^2 u_x}{\partial t^2} + \frac{(g-l)}{2} u_x + i\gamma |u_x|^2 u_x \\ & + i\gamma \frac{2|u_y|^2}{3} u_x + \frac{i\gamma u_x^* u_y^2}{3} + \frac{g}{2\Omega_g^2} \frac{\partial^2 u_x}{\partial t^2}, \end{aligned} \quad (1)$$

$$\begin{aligned} \frac{\partial u_y}{\partial z} = & i\beta u_y - \delta \frac{\partial u_y}{\partial t} - i\frac{\beta_2}{2} \frac{\partial^2 u_y}{\partial t^2} + \frac{(g-l)}{2} u_y + i\gamma |u_y|^2 u_y \\ & + i\gamma \frac{2|u_x|^2}{3} u_y + \frac{i\gamma u_y^* u_x^2}{3} + \frac{g}{2\Omega_g^2} \frac{\partial^2 u_y}{\partial t^2}, \end{aligned} \quad (2)$$

$$g = g_0 \exp \left[-\frac{\int_0^{T_R} |u_x|^2 + |u_y|^2 dt}{E_s} \right], \quad (3)$$

$$T = (1 - \alpha_{ns}) - \frac{\alpha_s}{1 - P/P_s}. \quad (4)$$

Here, u_x and u_y are slowly varying pulse envelopes propagating along the fast and slow axes of the fiber. z represents propagation distance, and t is the retard time. $\beta = \pi/L_b$, and $\delta = \lambda/2cL_b$ correspond to wave-number and inverse group velocity between two orthogonal-polarized components. $L_b = \lambda/B_m$ is the beat length, and B_m is the fiber birefringence. β_2 , γ , and l are the group-velocity dispersion, cubic refractive nonlinearity, and loss of fibers, respectively. Ω_g represents the full width at half maximum of the gain spectrum of EDF. g indicates the saturable gain, in which g_0 is the small signal gain coefficient and E_s is the gain saturation energy. T_R represents the time window of the simulation. Formula 4 shows the transfer function of the CNT-SA, where α_{ns} is the non-saturable absorption component, α_s is the modulation depth, P represents the instantaneous pulse power, and P_s represents the saturable power. When the pulse propagates to the CNT-SA, the optical fields are multiplied by the corresponding transfer function at the cavity position of 8.7 m. Based on the

experimental setup, the simulation parameters are set as $\lambda = 1560$ nm, $c = 3 \times 10^8$ m/s, $\Omega_g = 40$ nm, $l = 0.02$ dB/km, and $B_m = 0.9 \times 10^{-6}$. For the EDF, $\beta_2 = 23.6$ ps²/km and $\gamma = 3$ W⁻¹ km⁻¹. For the SMF, $\beta_2 = -21.6$ ps²/km, and $\gamma = 1$ W⁻¹ km⁻¹. The PMF parameters are consistent with the SMF, except for B_m of 3.8×10^{-4} . $g_0 = 3.93$ m⁻¹, $\alpha_{ns} = 0.51$, $\alpha_s = 8\%$, and $P_s = 15$ W.

The polarization orientation of the pulse before the PMF determines the operation state of the laser. For the saturation energy of 11.4 pJ, the fiber laser outputs a typical stretched pulse for θ of 0 or 0.5π , which is consistent with the results in Appendix A. When θ is 0.3π , we obtain the OSM from a noise pulse after 200 RTs. Without loss of generality, the pulses of two adjacent RTs (664th and 665th) are extracted for analysis [Figs. 3(a) and 3(b)]. The simulated spectra of OSMs exhibit a modulation of 5.67 nm, comparable with the experimental observation of 5.52 nm. To compensate for the birefringence-induced walk-off effect, the spectra of two orthogonal-polarized components shift in opposite directions in accord with Fig. 1(c). The autocorrelation traces have tri-peak structures [Figs. 3(c) and 3(d)], where the secondary peaks are less than half of the central peak, indicating that the OSM is composed of two unequal pulses. The pulse profiles in Figs. 3(e) and 3(f) further support our conclusion that the weak spectral modulation corresponds to the unequal pulses in the OSM. It is worth noting that the spectra and pulse profiles of two orthogonal-polarized components flip in two adjacent RTs, accompanied by the energy redistribution at the connection point of SMF and PMF.

The dynamic evolutions of the OSMs along the cavity at adjacent RTs are depicted in Fig. 4. Taking the 664th RT as an example [Fig. 4(a)], the OSM consists of two unequal pulses, in which the weaker one is in front of the stronger pulse at the initial state. In the PMF the stronger pulse splits in two parts in a ‘‘Y’’ manner while the weaker pulse couples to the stronger one, resulting in the OSM that the weaker pulse lies behind the stronger pulse. The pulse profiles are replotted in Figs. 4(a) and 4(b) for a clear demonstration. In the next

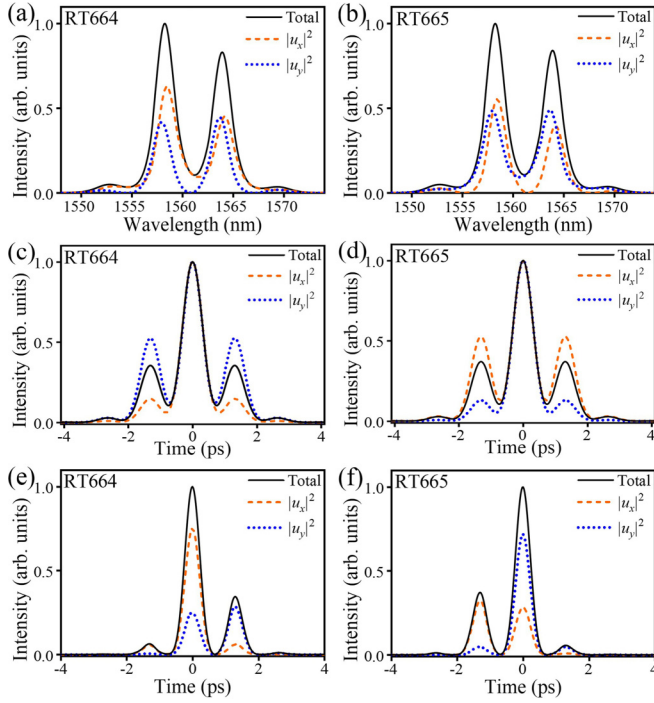


FIG. 3. Simulation results of OSMs at 664th and 665th RTs. (a), (b) Optical spectra. (c), (d) Autocorrelation traces. (e), (f) Pulse profiles. [Total: the solid black lines; u_x components: the dashed orange lines; u_y components: the dotted blue lines.]

RT, two pulses evolve similarly along the cavity, while their positions are opposite in the temporal domain.

Figures 4(c)–4(f) show the evolutions of two orthogonal-polarized components of OSMs. In the 664th RT, the u_x component is divided in two similar parts at the connection point of SMF and PMF. Meanwhile, the u_y component, consisting of two similar pulses, merges in a single pulse. The evolutions of two components in the 665th RT are opposite [Figs. 4(d) and 4(f)]. Considering the mode-coupling equation in Fig. 1(b), two orthogonal-polarized components in SMF couple energy unequally to the slow and fast axes of PMF

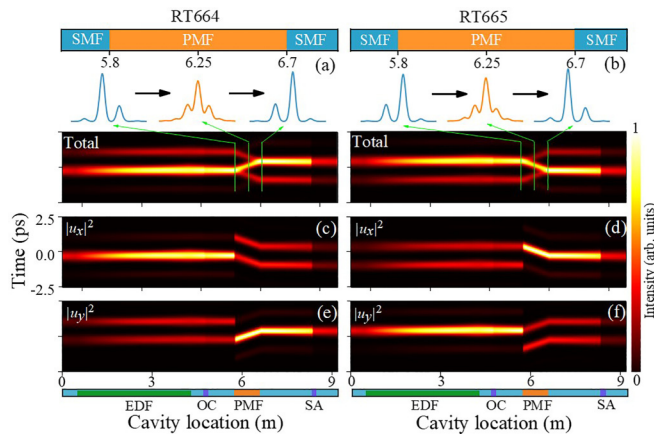


FIG. 4. Temporal evolutions of OSMs vs cavity position at 664th and 665th RTs. (a), (b) Total pulse and corresponding pulse profiles at 5.8 m, 6.25 m, and 6.7 m in the cavity; (c), (d) u_x component; (e), (f) u_y component.

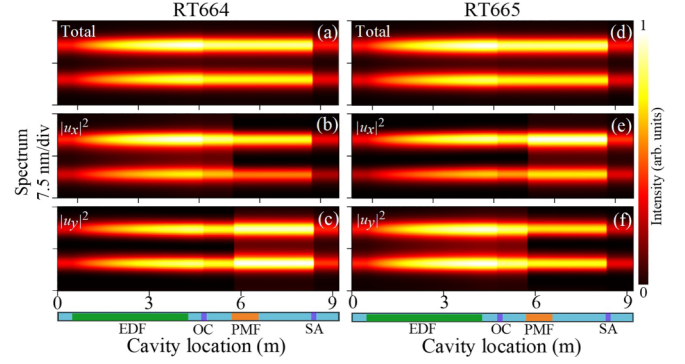


FIG. 5. Spectral evolutions of OSMs vs cavity position at 664th and 665th RTs. (a), (d) Total pulse; (b), (e) u_x component; (c), (f) u_y component.

for θ of 0.3π . Due to the strong birefringence of PMF, two components propagate upward and downward in the temporal domain. At the output terminal of PMF, the u_f and u_s components separately transform to u_x and u_y components in SMF, forming an OSM with the reversed pulse profile. With the assistance of the saturable absorption effect, two components evolve to the quasi-self-consistent state in the next circulation.

The spectral evolutions of OSMs are shown in Fig. 5. In the 664th RT [Fig. 5(a)], the OSM first passes through 0.5 m SMF and then enters 3.8 m EDF. The spectral intensity increases almost linearly in the front part while increasing slowly in the rear due to the saturable amplification property of the gain medium. Then the OSM is extracted by the 90:10 coupler and enters the 0.9-m-long PMF. Eventually, influenced by the nonsaturable loss of the CNT-SA, the OSM is sharpened and the spectral intensity decreases significantly. The evolution of the u_x (u_y) component at the 664th RT is similar to the u_y (u_x) component at the 665th RT. The spectral modulation depths change at the connection point of the SMF and PMF, which agrees with the temporal evolution shown in Fig. 4.

We further simulate the evolution of the OSMs and its two components over 100 RTs as illustrated in the three panels of Fig. 6. All of them display a large oscillation period of 27 RTs, compared to the experimental value of 29 RTs. The evolutions of the u_x and u_y components are similar to that of OSM, with small-period oscillations occurring per two RTs. In the temporal domain, two unequal pulses propagate in the cavity, accompanied by an obvious periodic oscillation. Two components exhibit a fusiform energy oscillation with a period of 27 RTs [right panels of Figs. 6(d) and 6(f)]. The averaged spectra and pulse profiles are plotted on the upper panels of Figs. 6(a)–6(f), matching the experimental results. Since the weaker pulse appears alternatively on the right and left sides of the stronger pulse, the averaged pulse profiles can be regarded as the appearance probability of two pulses. Our results indicate that the weaker pulses appear with the same probability on both sides. The corresponding autocorrelation traces are given in Appendix B, which also match the experimental results in Fig. 2.

The pulse profiles of OSMs over 27 RTs are extracted to reveal the underlying mechanism of the large-period oscillation. In each RT, the weaker pulse flips from one side of the stronger pulse to the other, resulting in the dual-roundtrip os-

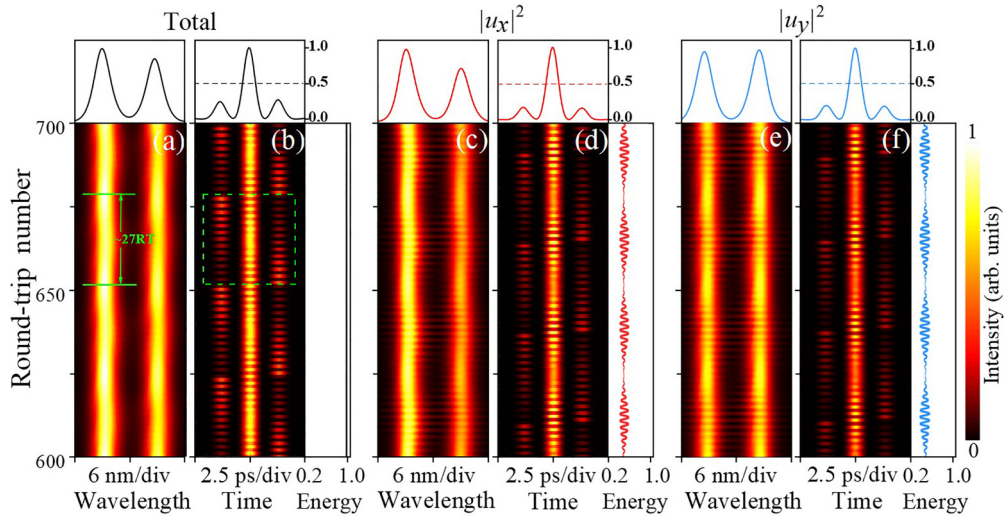


FIG. 6. Simulated evolution of OSMs over 600–700 RTs. Spectra and pulse profiles of (a), (b) total pulse, (c), (d) u_x component, and (e), (f) u_y component. Upper panels show the averaged spectra and pulse profiles. Right panels of (b), (d), and (f) show the evolution of the normalized energy.

cillation [Fig. 7(a)]. The peak ratios indicate the ratio of peak intensity between the weaker and stronger pulses. The blue and orange curves represent peak ratios of the weaker pulses on the upper and lower sides with respect to the stronger

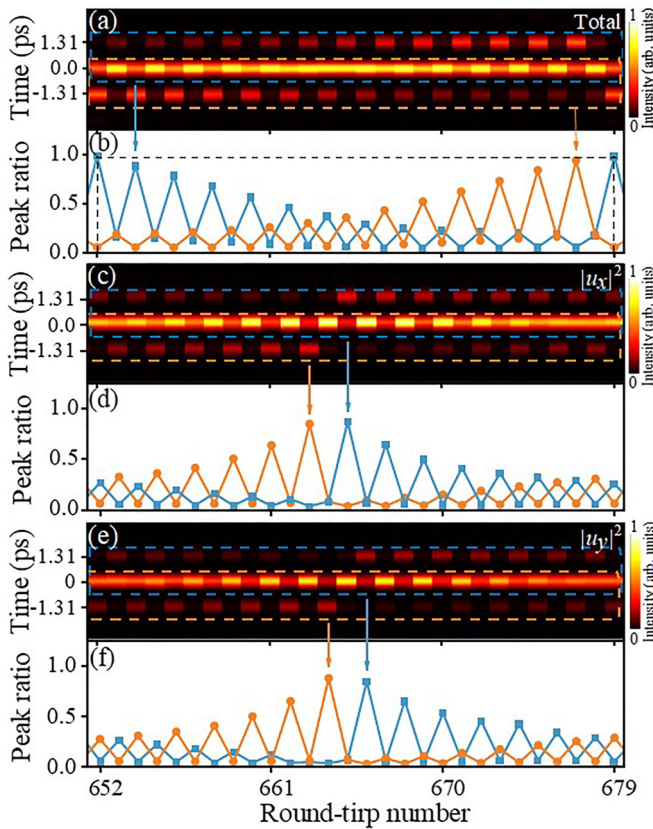


FIG. 7. Simulated evolution of OSMs over 652–679 RTs. Pulse profiles and peak ratios (blue squares and orange circles) between stronger pulse and weaker pulse of (a), (b) total pulse, (c), (d) u_x component, and (e), (f) u_y component.

pulse. Interestingly, the peak ratios change significantly per RT and display the opposite evolution trends, as shown in Fig. 7(b). However, the separation between two pulses is almost invariant with vibrations of less than 0.02 ps. The sawtoothlike peak ratios not only demonstrate the dual-roundtrip oscillation of the OSM but also verify the persistent variation of pulse intensity induced by strong vector-mode coupling. The two orthogonal-polarized components show similar evolution trends as the total pulse. However, the weaker pulses of the two components are at inverse positions of adjacent RTs [Figs. 7(c)–7(f)]. The OSM and two components recover at the 679th RT with the same property as the initial state and enter the next circulation.

Based on the above results, the formation of OSM can be understood as follows. According to vector-mode coupling theory, the intensities of two orthogonal-polarized components depend on the pulse polarization states before the PMF, which are unequal in most cases. Attributed to the birefringence-induced walk-off effect, two components continuously depart and couple in the PMF, resulting in the dual-roundtrip oscillation that the weaker pulse jumps back and forth around the stronger pulse. Besides, the OSM and its two components evolve back to the same state over the large-period oscillation. The period of such oscillation changes with the coupling angle, differing from Hopf-type bifurcation-induced oscillation that depends on the pump power.

IV. CONCLUSION

We demonstrate a type of OSMs with intriguing internal dynamics in a near-zero-dispersion SMF-PMF laser. Two constituent pulses of OSMs possess different intensities, and the weaker pulse jumps back and forth around the stronger one. Attributed to the unequal coupling and walk-off effect of PMF, the stronger pulse splits into two pulses for one orthogonal-polarized component, while two weaker pulses merge in a stronger pulse for the other orthogonal-polarized component inside the cavity. Real-time spectral results show

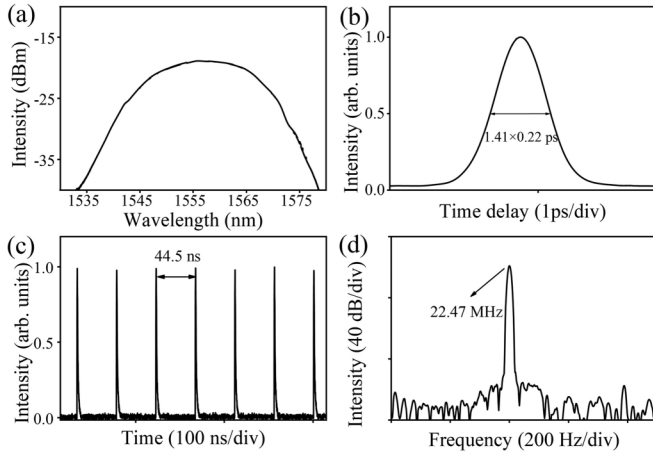


FIG. 8. Experimental results of the stretched pulse: (a) optical spectrum, (b) autocorrelation trace, (c) pulse train, and (d) radio-frequency spectrum.

that such unequal vector-mode coupling determines the dual-roundtrip oscillation and the large-period oscillation. Our results provide a practical approach to generate controllable OSMs with the assistance of PMF.

ACKNOWLEDGMENTS

This work was funded by the National Natural Science Foundation of China under Grants No. 11874300 and No. 12274344, and the Natural Science Foundation of Shaanxi Province under Grant No. 2019JQ-447.

APPENDIX A: STRETCHED PULSE

In the near-zero dispersion of the SMF-PMF laser, we first obtain a stretched pulse by adjusting the PC, as shown in Fig. 8. The output pulse displays the characteristic broadband

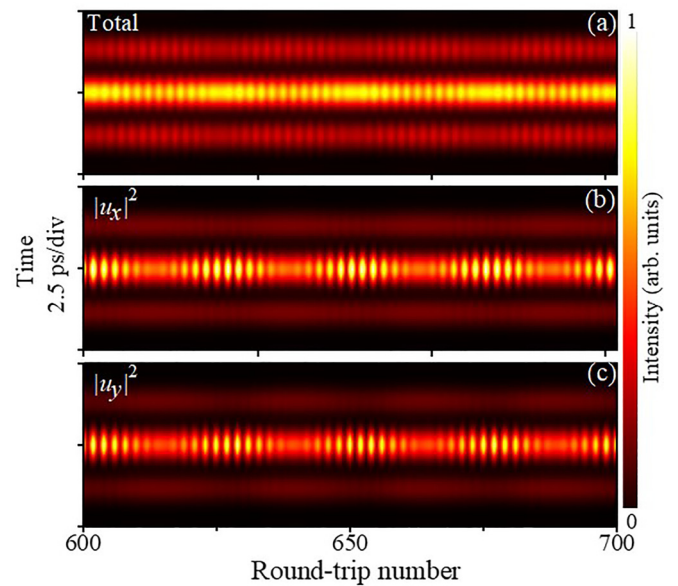


FIG. 9. Autocorrelation traces of OSM over 600–700 RTs: (a) total pulse, (b) u_x component, and (c) u_y component.

spectrum with a duration of 220 fs. Based on the pulse train and the radio-frequency spectrum, we verify that the fiber laser delivers stable single-pulse mode-locking.

APPENDIX B: AUTOCORRELATION TRACE OF OSM IN FIG. 6

Figure 9 shows the autocorrelation traces of OSM, which is similar to the experimental results [Figs. 2(b), 2(d), and 2(f)]. Apart from the large-period oscillation of 27 RTs, there is a small-period oscillation where the intensity of pulses changes significantly per two RTs.

- [1] T. Dauxois and M. Peyrard, *Physics of Solitons* (Cambridge University Press, Cambridge, England, 2015).
- [2] A. S. Davydov, *J. Theor. Biol.* **66**, 379 (1977).
- [3] M. Borghesi, S. Bulanov, D. H. Campbell, R. J. Clarke, T. Zh. Esirkepov, M. Galimberti, L. A. Gizzi, A. J. MacKinnon, N. M. Naumova, F. Pegoraro *et al.*, *Phys. Rev. Lett.* **88**, 135002 (2002).
- [4] D. R. Solli, C. Ropers, P. Koonath, and B. Jalali, *Nature (London)* **450**, 1054 (2007).
- [5] S. K. Turitsyn, B. G. Bale, and M. P. Fedoruk, *Phys. Rep.* **521**, 135 (2012).
- [6] P. Grelu and N. Akhmediev, *Nat. Photonics* **6**, 84 (2012).
- [7] J. Peng, Z. Zhao, S. Boscolo, C. Finot, S. Sugavanam, D. V. Churkin, and H. Zeng, *Laser Photonics Rev.* **15**, 2000132 (2021).
- [8] D. Tang, L. Zhao, B. Zhao, and A. Liu, *Phys. Rev. A* **72**, 043816 (2005).
- [9] N. N. Akhmediev and A. Ankiewicz, *Phys. Rev. Lett.* **79**, 4047 (1997).
- [10] B. A. Malomed, *Phys. Rev. A* **44**, 6954 (1991).
- [11] A. B. Grudinin and S. Gray, *J. Opt. Soc. Am. B* **14**, 144 (1997).
- [12] C. Bao, X. Xiao, and C. Yang, *Opt. Lett.* **38**, 1875 (2013).
- [13] S. Chouli and P. Grelu, *Phys. Rev. A* **81**, 063829 (2010).
- [14] A. Klein, G. Masri, H. Duadi, K. Sulimany, O. Lib, H. Steinberg, S. A. Kolpakov, and M. Fridman, *Optica* **5**, 774 (2018).
- [15] A. Zavyalov, R. Iliew, O. Egorov, and F. Lederer, *Phys. Rev. A* **80**, 043829 (2009).
- [16] A. Hause, H. Hartwig, B. Seifert, H. Stolz, M. Böhm, and F. Mitschke, *Phys. Rev. A* **75**, 063836 (2007).
- [17] A. Komarov, H. Leblond, and F. Sanchez, *Phys. Rev. E* **72**, 025604 (2005).
- [18] S. G. Evangelides, L. F. Mollenauer, J. P. Gordon, and N. S. Bergano, *J. Lightwave Technol.* **10**, 28 (1992).
- [19] Y. Du, Q. Gao, J. Li, C. Zeng, D. Mao, and J. Zhao, *Opt. Lett.* **46**, 5599 (2021).
- [20] Z. Wang, K. Nithyanandan, A. Coillet, P. Tchofo-Dinda, and P. Grelu, *Nat. Commun.* **10**, 830 (2019).

- [21] J. Peng and H. Zeng, *Opt. Lett.* **44**, 2899 (2019).
- [22] B. Ortaç, A. Zaviyalov, C. K. Nielsen, O. Egorov, R. Iliew, J. Limpert, F. Lederer, and A. Tünnermann, *Opt. Lett.* **35**, 1578 (2010).
- [23] Y. Du, Q. Gao, Z. He, J. Li, C. Zeng, D. Mao, and J. Zhao, *Phys. Rev. A* **104**, 043508 (2021).
- [24] D. Tang, W. S. Man, H. Y. Tam, and P. D. Drummond, *Phys. Rev. A* **64**, 033814 (2001).
- [25] X. Wang, J. He, B. Mao, H. Guo, Z. Wang, Y. Yue, and Y. G. Liu, *Opt. Express* **27**, 28214 (2019).
- [26] P. Rohrmann, A. Hause, and F. Mitschke, *Phys. Rev. A* **87**, 043834 (2013).
- [27] M. Liu, Z. Wei, H. Li, T. Li, A. Luo, W. Xu, and Z. Luo, *Laser Photonics Rev.* **14**, 1900317 (2020).
- [28] K. Goda and B. Jalali, *Nat. Photonics* **7**, 102 (2013).
- [29] J. Igbonacho, K. Nithyanandan, K. Krupa, P. T. Dinda, P. Grelu, and A. B. Moubissi, *Phys. Rev. A* **99**, 063824 (2019).
- [30] J. Peng and H. Zeng, *Laser Photon. Rev.* **12**, 1800009 (2018).
- [31] Y. Zhou, Y. Ren, J. Shi, H. Mao, and K. K. Y. Wong, *Optica* **7**, 965 (2020).
- [32] K. Krupa, K. Nithyanandan, U. Andral, P. Tchofo-Dinda, and P. Grelu, *Phys. Rev. Lett.* **118**, 243901 (2017).
- [33] M. Grapinet and P. Grelu, *Opt. Lett.* **31**, 2115 (2006).
- [34] J. M. Soto-Crespo, P. Grelu, N. Akhmediev, and N. Devine, *Phys. Rev. E* **75**, 016613 (2007).
- [35] W. He, M. Pang, D. H. Yeh, J. Huang, C. R. Menyuk, and P. S. J. Russell, *Nat. Commun.* **10**, 5756 (2019).
- [36] M. N. Islam, C. D. Poole, and J. P. Gordon, *Opt. Lett.* **14**, 1011 (1989).
- [37] S. T. Cundiff, B. C. Collings, N. N. Akhmediev, J. M. Soto-Crespo, K. Bergman, and W. H. Knox, *Phys. Rev. Lett.* **82**, 3988 (1999).
- [38] L. M. Zhao, D. Y. Tang, X. Wu, H. Zhang, and H. Y. Tam, *Opt. Lett.* **34**, 3059 (2009).
- [39] Y. Du and X. Shu, *Opt. Express* **25**, 28035 (2017).
- [40] Z. Wu, Q. Wei, P. Huang, D. Luo, X. Zhang, S. Fu, L. Zhao, D. Liu, P. Shum, and T. Huang, *Opt. Express* **28**, 5212 (2020).
- [41] D. Mao, X. Liu, and H. Lu, *Opt. Lett.* **37**, 2619 (2012).
- [42] K. Tamura, E. P. Ippen, H. A. Haus, and L. E. Nelson, *Opt. Lett.* **18**, 1080 (1993).
- [43] P. Wang, C. Bao, B. Fu, X. Xiao, P. Grelu, and C. Yang, *Opt. Lett.* **41**, 2254 (2016).
- [44] D. Mao, Z. He, Y. Zhang, Y. Du, C. Zeng, L. Yun, Z. Luo, T. Li, Z. Sun, and J. Zhao, *Light: Sci. Appl.* **11**, 25 (2022).
- [45] D. Mao, Z. He, Q. Gao, C. Zeng, L. Yun, Y. Du, H. Lu, Z. Sun, and J. Zhao, *Ultrafast Sci.* **2022**, 9760631 (2022).
- [46] G. P. Agrawal, *Nonlinear Fiber Optics* (Springer, Berlin Heidelberg, 2007).